Lithium intercalation mechanism and critical role of structural water in layered $H_2V_3O_8$ high-capacity cathode material for lithium ion batteries

A. Kuhn[*,§], J.C. Pérez-Flores[‡], J. Prado-Gonjal[¥], E. Morán[¥,†], M. Hoelzel[#], V. Díez-Gómez[$], I. Sobrados[$], J. Sanz[$], F. García-Alvarado[§]

[§] Departamento de Química y Bioquímica, Facultad de Farmacia, Universidad San Pablo CEU, CEU Universities, Urbanización Montepríncipe, 28668 Boadilla del Monte, Madrid, Spain

[‡] Instituto de Investigación de Energías Renovables, Universidad de Castilla-La Mancha, Albacete, Spain

[¥] Universidad Complutense de Madrid, Departamento de Química Inorgánica, Facultad de Ciencias Químicas, Ciudad Universitaria s/n, 28040 Madrid, Spain

[#] Forschungsneutronenquelle Heinz-Maier-Leibniz (FRM II), Technische Universität München, Lichtenbergstrasse 1, D-85747 Garching, Germany

[$] Instituto de Ciencia de Materiales Madrid (CSIC), 28049 Cantoblanco, Madrid, Spain

[†] Deceased on April 16th, 2020

ABSTRACT

$H_2V_3O_8$ (HVO) is a promising high-capacity cathode material for lithium-ion batteries (LiB). It allows reversible two-electron transfer during electrochemical lithium cycling processes yielding a very attractive theoretical capacity of 378 mAh g^{-1}. While an abundant number of research works exclusively proved the outstanding electrochemical lithium storage properties of $H_2V_3O_8$, structural changes during the intercalation process have not been scrutinized, and the crystallographic positions occupied by the guest species have not been revealed yet. However, an in-depth understanding of structural changes of cathode materials is essential in developing new materials and improving current materials. Aimed at providing insight into the storage behavior of HVO, in this work we employed a combination of high-resolution synchrotron X-ray and neutron diffraction to accurately describe the crystal structures of both pristine and lithiated $H_2V_3O_8$. In HVO, hydrogen is located on one single-crystallographic site in a water-like arrangement, through which bent asymmetric hydrogen bonds across adjacent $V_3O_8^{2-}$ chains are established. The role played by water on the network stabilization was further examined by DFT calculations. Easy hydrogen-bonding switch of structural water upon lithium intercalation not only allows a better accommodation of intercalated lithium ions, but also enhances Li-ion mobility in the crystal host, as evidenced by MAS-NMR spectroscopy. Facile conduction pathways for Li ions in the structure are deduced from bond valence sum difference mapping. The hydrogen bonds mitigate the volume expansion/contraction of vanadium layers during Li intercalation/deintercalation, resulting in improved long-term structural stability, explaining the excellent performance in rate capability and cycle life reported for this high-energy cathode in LIBs. This study suggests that many hydrated materials can be good candidates for electrode materials not only of implemented Li technology, but also emerging rechargeable batteries.

Keywords: High-energy density lithium battery, cathode $H_2V_3O_8$, hydrogen bonding, NMR spectroscopy, SXRD, neutron diffraction, DFT calculations.

INTRODUCTION

In the current global context of continuous search of reliable and clean energy sources applicable for smart grids, electric vehicles and portable electronic devices, lithium storage batteries appear to be the most appealing option. Vanadium oxides and related compounds are considered as competitive, potentially alternative cathode materials to current state-of-the-art $LiCoO_2$ due to their large specific capacity and abundant sources .[1-5] Most of research activity on vanadium oxides has been focused on morphology to improve electrochemical performances. Several one-dimensional nanostructures such as nanobelts,[6-8] nanorods,[5] nanosheets,[9] nanowires[10] and nanowire bundles[11] have been described. The final morphology not only depends on the synthetic procedures employed: precipitation, sol-gel, electrodeposition, micellar reverse technique, or hydrothermal methods,[7,8, 11-16] but also on the nature of additives in the reactant media[17]. Such nanoarchitectures are ideal because they simultaneously provide high electrode-electrolyte interface area, good structural stress release and improved lithium-ion diffusion.[18-20]

Among layered vanadium oxides, hydrated vanadium oxide $H_2V_3O_8$ (or $V_3O_7{\cdot}H_2O$) showed its potential as promising high-capacity (378 $mAh{\cdot}g^{-1}$) and high-energy (945 $Wh{\cdot}kg^{-1}$ at an average voltage of 2.5 V) cathode material for lithium-ion batteries.[11, 21-23] Moreover, it is one of the few materials able to intercalate more than one specific guest ion (Li^+, Na^+, K^+, Mg^{2+} or Zn^{2+}) with substantial capacities.[24-28] Additional efforts have been made to improve its rate capability and low electrical conductivity using composite electrodes with carbon-based materials such as graphene[29-31] and its cycle stability by surface coating with aluminum oxyhydroxide.[32] Preintercalation has been recently demonstrated as interesting strategy to further enhance the electrochemical performance of $H_2V_3O_8$ for Li^+ and Na^+ insertion.[33,34]

First synthesized by Theobald and Cabala[35], its heavy atom crystal structure was determined by Oka et al.[36] and improved further by Mettan et al.[37] However, neither hydrogen occupancy nor the chemical role that hydroxyl groups/coordinated water molecules play in the structural framework could be undoubtedly established.

In a previous work we synthesized $H_2V_3O_8$ nanobelts by means of an innovative, easy, cost-effective, and environmentally respectful microwave-assisted hydrothermal method, while maintaining the characteristic electrochemical features.[22] Our XRD and HRTEM analysis showed that $H_2V_3O_8$ crystallizes in the *Pnma* (#62) orthorhombic system (a = 16.809(2) Å, b = 3.62444(5) Å and c = 9.303(1) Å).[27] $H_2V_3O_8$ is considered a promising electrode material with enhanced electrochemical performance compared to other vanadium-based oxides, because of a higher electronic conductivity[38] arising from the reduced oxidation state of vanadium (+4.67, V^{5+}/V^{4+} = 2:1 ratio) as deduced from EELS, and the vanadium atoms being electrochemical redox centers. Two IR bands at ~ 3416 and 1637 cm^{-1} were ascribed to stretching –OH and bending H_2O modes, respectively, of structural coordination water.

In this structure, hydrogen bonds between vanadium layers provide an elastic buffer space to mitigate the volume expansion/contraction of vanadium layers during the Li intercalation and deintercalation process, thus maintaining the high capacity and good cycling stability.[11, 39] $H_2V_3O_8$ develops a high discharge capacity of 378 mAh g^{-1} corresponding to approximately 4 Li^+ ions in the 3.75-1.50 V voltage range (Fig. 1, left).[22] The lithium insertion curve is governed by a series of sloping voltage regions alternated with constant voltage regions, characteristic for single-phase solid solutions and two-phase domains, respectively.[22] The incremental capacity curve (Fig. 1, right) shows four reversible peaks centered at 3.20, 2.75, 2.30 and 1.90 V vs. Li^+/Li. Recently, Wu et al. investigated the electrochemical lithium intercalation and de-intercalation in $H_2V_3O_8$

nanorods by *in situ* TEM, confirming an intercalation mechanism upon initial lithiation down to 1.5 V vs. Li^+/Li with a capacity of 215 mAh g^{-1}.[39] Subsequent lithiation in the lower voltage range 1.5 - 0.2 V resulted in a localized intermediate VO_2 phase, which is further converted into a V_2O_3 phase. The localized phase transformation between the VO_2 phase and $V_2O_3 + Li_2O$ phases was reversible during subsequent cycles.

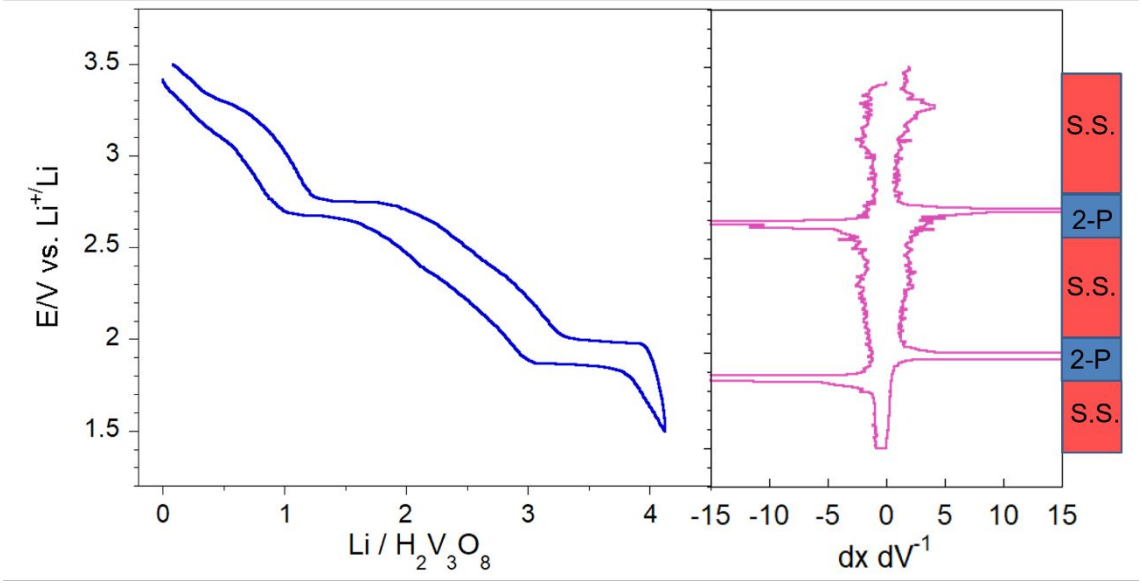

Fig. 1. Electrochemical galvanostatic discharge-charge profile of a $H_2V_3O_8$//Li cell at C/20 rate in the 3.75-1.50 V range (left). Incremental capacity curve $(dV/dx)^{-1}$ showing the presence of four main electrochemical features (right).

However, although a considerable number of papers have been published about the electrochemical performance of $H_2V_3O_8$ in Li batteries in the last decade, the structural and chemical changes $H_2V_3O_8$ undergoes upon lithium intercalation are not understood so far. In particular, crystallographic sites that hydrogen and lithium occupy in intercalated $H_2V_3O_8$ have not been revealed yet, and little work has been reported to date on how structural water contributes to the electrochemical performance.

In this work, we decided to undertake a detailed study of structural changes during Li intercalation of 1 Li^+/f.u. Note that lithium insertion in $H_2V_3O_8$ begins with a solid solution domain for the compositional range $0 \leq x \leq 1$ (Fig. 1). First, we prepared polycrystalline lithium intercalated samples by chemical lithiation up to x = 1 and determined their precise crystal structure. The complementary use of SXRD and NPD was especially effective in $Li_xH_2V_3O_8$ compounds because neutrons have little sensitivity to vanadium (contrary to X-rays), whereas X-rays have low sensitivity to lithium and hydrogen (contrary to neutrons). Fourier neutron density analysis was used to determine the positions of both hydrogen and lithium ions. Bond valence sum (BVS) mapping calculations were used to provide additional support for lithium-ion diffusion in the structure. Refined structural models of both pristine and intercalated samples were reexamined by means of DFT calculations, with special emphasis on Li and H positions. The structural analysis was completed by investigation of the role played by OH/coordinated water in structural stabilization. The allocation and mobility of Li^+ ions were analyzed by means of neutron diffraction, DFT and solid-state MAS-NMR techniques.

EXPERIMENTAL SECTION

Synthesis of $H_2V_3O_8$ nanobelts

Synthesis of $H_2V_3O_8$ was done in a Milestone ETHOS 1 system as previously reported,[22] using V_2O_5 (0.5 mmol, Aldrich, 98%) and ethanol (5 ml, Scharlau, synthesis grade) as reactants mixed in distilled water. The mixture was heated at 200ºC for 2 h (heating ramp 10 ºC/min) while microwave radiation was set at 2.45 GHz (maximum power limited to 500 W) and inner pressure is maintained at ~21 bars during the highest temperature

period. In the microwave-assisted synthesis, vanadium is reduced from V^{5+} to $V^{4.67+}$, (V^{5+}/V^{4+} = 2:1 ratio). The as-obtained product was washed with water and dried at 80ºC to yield pure $H_2V_3O_8$ green nanobelts in the 100 nm to few tens micrometers length range.

Synthesis of lithiated $Li_xH_2V_3O_8$ materials

The positive electrode was prepared by mixing $H_2V_3O_8$, conductive carbon C65-Timcal and PVdF binder in the 85:10:5 weight ratio and pressing the mixture into 8 mm diameter pellets, followed by drying overnight at 80ºC. A lithium inserted $Li_xH_2V_3O_8$ sample, with a precise lithium content x = 1, suitable for synchrotron X-ray diffraction studies, was synthetized by discharging a lithium half-cell from its *open-circuit voltage* to 2.75 V vs. Li^+/Li, corresponding to the end stage of the first solid-solution domain observed in the electrochemical discharge curve. The electrochemical cell was composed of positive electrode, glass fiber separator (Whatman) soaked with 1 M $LiPF_6$ in ethylene carbonate (EC) and dimethyl carbonate (DMC) (1:1 vol %) as electrolyte, and Li metal as negative electrode, assembled in CR2032-type coin cells. The cell was discharged under potentiostatic conditions to the aforesaid voltage and left to equilibrate until the measured current was < 0.1 μA. The cell was then stopped and disassembled in an argon-filled glovebox. Electrolyte was removed by washing the positive electrodes with dry DMC. To avoid exposition to moisture or oxygen, the lithiated sample was sealed under inert atmosphere in a borosilicate capillary.

A lithium intercalated sample with nominal composition x = 1, suitable for neutron powder diffraction, was prepared by chemical lithiation of $H_2V_3O_8$ with the corresponding stoichiometric amount of a 1.6 M n-butyllithium solution (Aldrich). Only for NMR studies, another sample with nominal composition x = 0.5 was prepared applying the same chemical lithiation procedure. The $H_2V_3O_8$ powder was first suspended

with a small amount of anhydrous hexane, and n-butyllithium solution was slowly added while stirring the mixture. The reaction mixtures were stirred for 2 weeks at room temperature, samples were filtered, washed repeatedly with dry hexane, and finally dried under vacuum. All sample preparations were carried out in an argon-filled glovebox to prevent reaction of the lithiated compounds with air and moisture. The chemical lithiation is accompanied by a color change of the oxide from green to dark blue. Lithium contents of the two lithiated samples were deduced by Atomic Emission Spectroscopy (AES) confirming nominal compositions.

Structural Analysis

High-resolution synchrotron XRD diffraction experiments were carried out at the SpLine beamline (BM25A) of the Spanish CRG at ESRF (Grenoble, France). The pristine $H_2V_3O_8$ and a lithiated sample with composition x = 1.0 were measured at 300 K in the 2θ angular range 3-30º, using the wavelength λ = 0.49684 Å and rotating capillaries. The contribution from the V atoms (69 electrons in the formula unit) to the X-ray scattering is approximately the same as that of the O atoms (64 electrons). The ND neutron scattering by V atoms (b = -0.382 fm) is insignificant in comparison to oxygen scattering (b = 5.803 fm), which favors the location of O in the unit cell with higher accuracy. Furthermore, the negative neutron scattering length factor of Li increases considerably their contrast with respect to O atoms in Fourier density maps. For this reason, high angular resolution neutron powder diffraction (NPD) patterns of the x = 1.0 sample were recorded at 300 K in SPODI at Heinz Maier-Leibnitz source FRM II, Garching, Germany.[40] NPD patterns were recorded in the 2θ angular range 3-150º using the wavelength 1.54827 Å selected with a Ge(551) monochromator. Samples were loaded in

argon atmosphere in airtight vanadium cans sealed with indium O-rings to prevent them from reaction with moisture and air.

All diffraction patterns were analyzed, and crystal structures determined by the Rietveld method using the FullProf program,[41] where the initial structural model for $H_2V_3O_8$ was taken from previous reports.[36] In Rietveld refinements of structural model parameters from synchrotron X-ray diffraction data, an anisotropic broadening of diffraction peaks, owing to the acicular morphology of pristine and lithiated $H_2V_3O_8$ compounds, was considered using spherical harmonics expansion of the crystallite shapes as implemented in Fullprof.[41] The size-model 18 with Laue class *mmm* was selected.

The position of hydrogen and lithium was confirmed from neutron-density ND maps calculated with neutron diffraction patterns of $H_2V_3O_8$ and $LiH_2V_3O_8$. Fourier density difference maps were built using the GFourier package incorporated in Fullprof.[41] The coherent neutron scattering lengths used were: V: –0.3824 fm, Li: –1.90 fm, O: +5.803 fm and H: -3.7390 fm.[42] BVS maps were obtained utilizing the BVS Mapping package incorporated in Fullprof.[41] Structural models were visualized using the Vesta 3.3 software.[43]

Magnetic characteristics were measured with a SQUID magnetometer (MPMS-XL, Quantum Design). For that, the temperature dependence of the magnetization was registered in pristine and lithiated samples. Initially, around 20 mg of $H_2V_3O_8$ and $LiH_2V_3O_8$ powder synthesized by the microwave-hydrothermal method were cooled down to 5 K with no applied magnetic field. Zero field cooling (ZFC) data were collected at 0.1 T. Afterwards, the samples were cooled down again with the applied magnetic field of 0.1T and field cooled (FC) data recorded. Moreover, magnetization curves were collected at 5 K and 300 K by cycling magnetic field between ±5 T.

Morphology and shape of the pristine sample was studied by field-emission scanning electron microscopy (FE-SEM) and transmission electron microscopy (TEM) by using JEOL 6335F and JEOL JEM 2100 microscopes, respectively. Micrographs of $H_2V_3O_8$ nanobelts are included in the Supporting Information file (Fig. S1). They present a width of ca. 50-200 nm and a length of a few micrometres.

DFT calculations

Density Functional Theory (DFT) calculations were carried out using the CASTEP code,[44] which employs the gauge including projector augmented wave (GIPAW)[45] algorithm, enabling the reconstruction of the all-electron wave function in the presence of a magnetic field. The Generalized Gradient Approximation (GGA) PBE[46] functional was used, and the core-valence interactions were described by ultrasoft pseudopotentials.[47] Geometry optimization was performed on structures deduced by synchrotron X-ray diffraction, allowing to vary the atomic coordinates while keeping experimental values for unit cell parameters. Wavefunctions were expanded in planewaves with kinetic energy below the cut-off energy 1200 eV and integrals over the Brillouin zone were performed using a Monkhorst–Pack grid with a k-point spacing of 0.04 $Å^{-1}$. Optimizations were pursued until energy difference, maximum atomic force and maximum atomic displacement fell below tolerances of $1 \cdot 10^{-6}$ eV $atom^{-1}$, $3 \cdot 10^{-2}$ eV $Å^{-1}$ and $1 \cdot 10^{-3}$ Å, respectively.

MAS NMR spectroscopy

^{51}V, ^{7}Li and ^{1}H MAS NMR spectra were recorded at room temperature in an AVANCE-400 Bruker spectrometer, at 105.25, 155.50 and 400.13 MHz (9.4 T). NMR spectra were obtained after single pulse $\pi/2$ irradiation (2.5, 1.8 and 5 μs) with a recycling

time of 10s (^{51}V) and 5s (^{7}Li and ^{1}H). Samples were spun in 4 mm ZrO_2 rotors at 10 kHz around an axis inclined at 54°44' with respect to the magnetic field (magic-angle spinning technique, MAS). From spectra recorded at increasing spinning rates, isotropic chemical shift values were deduced from bands that do not change with the spinning rate. The number of scans was chosen to get signal/noise ratios higher than 10. ^{51}V, ^{7}Li and ^{1}H chemical shifts values were reported relative to vanadium pentoxide in 5% HCl solution, 1 M LiCl solution and acetone as secondary reference relative to TMS. To study the Li-H interaction, CP-MAS experiments were performed in lithiated samples. A contact time of 1 ms and a recycling delay of 5 s was used for these experiments.

Depending on the nuclear spin, different interactions modulate NMR spectra. In the case of ^{1}H (I=1/2) chemical shift and dipolar interactions are present, but in ^{7}Li (I=3/2) and ^{51}V (I=7/2) NMR spectra, besides dipolar and chemical shift interactions, quadrupolar interactions are present. In samples with V^{4+} cations, paramagnetic interactions considerably broaden NMR spectra. The MAS-NMR technique improves resolution, and the experimental envelopes are modulated by equally spaced spinning sidebands. The NMR spectra analysis can provide information about chemical shift (δ_0, $\Delta\sigma$ and η), quadrupolar (C_Q and η) and dipolar (linewidth $\Delta\omega$) interactions. From spectra recorded at low spinning rates, anisotropic interactions can be deduced with the DMFIT software.[46] In presence of paramagnetic interactions, isotropic (δ_0) and anisotropic ($\Delta\omega$) terms are preponderant.

In-situ variable temperature experiments were performed to analyze the onset of local Li motions. In absence of Li motions, the position of Li components, mainly affected by paramagnetic interactions, follow a linear variation with inverse temperature.

RESULTS AND DISCUSSION

Characterization of as prepared $H_2V_3O_8$

Crystal structure

The synchrotron X-ray diffraction pattern of the green powder obtained by the microwave-hydrothermal procedure was completely indexed with space group *Pnma* (#62). Refined lattice parameters a = 16.8600(4) Å, b = 3.63388(8) Å, c = 9.3325(2) Å, V = 571.78 Å^3 were in good agreement with previously reported values for $H_2V_3O_8$ in literature.[22, 36] Positions and atomic displacement factors of the vanadium atoms were taken from the Rietveld refinement and fixed for the following structural refinements from powder neutron diffraction data, because its nucleus scarcely scatters neutrons.[42] Synchrotron X-ray and neutron diffraction patterns and their corresponding differences between observed and calculated profiles are shown in Fig. 2a and 2b. The position of hydrogen atoms was deduced by difference Fourier neutron density maps in $H_2V_3O_8$ using the powder ND data collected at 300K. Fig. 2c shows the Fourier difference map of the y = 0 section (xz plane), where negative residual peaks detected at the 8*d* position (~0.25 ~0 ~0.15) were ascribed to H atoms.

Crystal data and refined atomic parameters are reported in Table S1 and interatomic distances depicted in Table S2. At 300 K, only one hydrogen position (8*d*) was detected close to O6 in contrast to previous results.[37] The refinement of H atoms occupancy converged to values close to 1.0. The $H_2V_3O_8$ structure exhibits subtle differences with respect to that previously reported,[37] which could be associated with different synthesis routes used: microwave-assisted hydrothermal reaction with V_2O_5 as starting material subjected to partial reduction (this work), and hydrothermal reaction with $VOSO_4$ as starting reactant subjected to partial oxidation.[37]

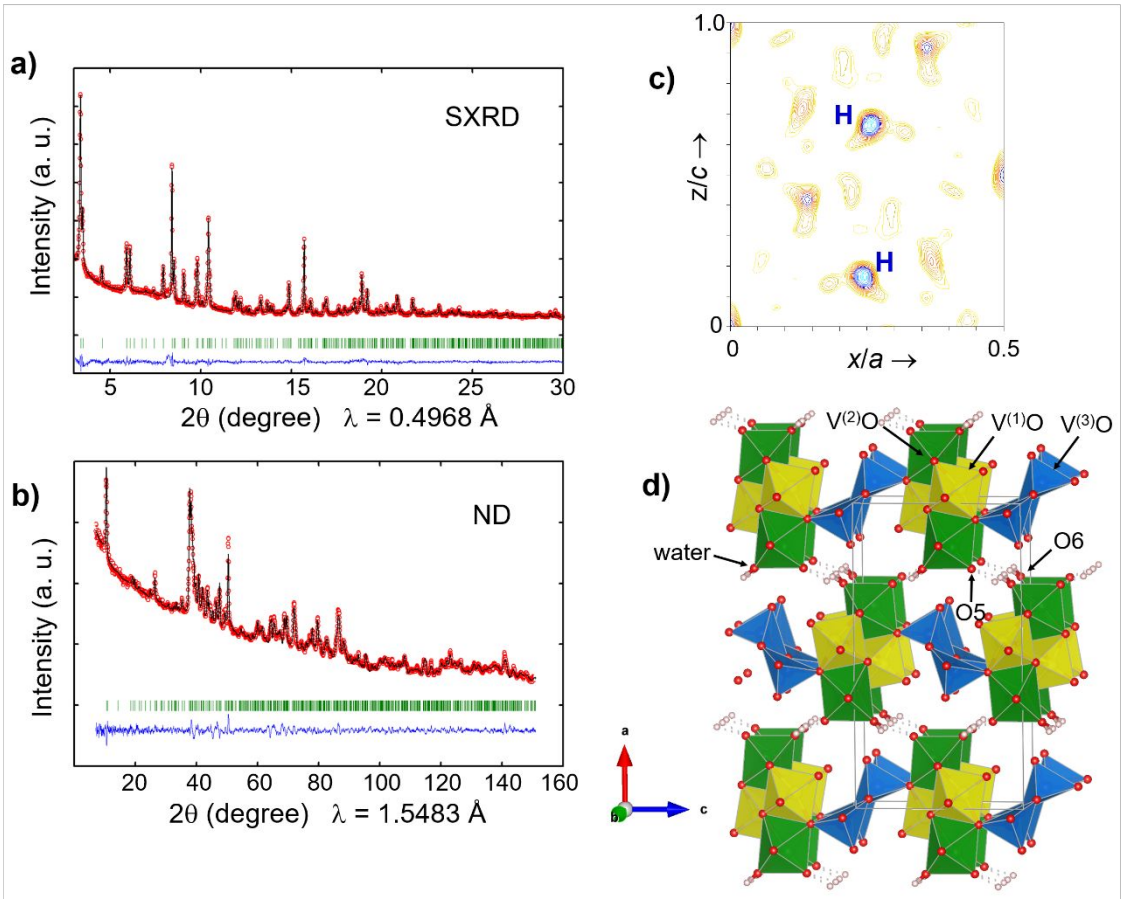

Fig. 2. The powder synchrotron X-ray (a) and neutron (b) Rietveld refinement profile for $H_2V_3O_8$ at 25ºC. Observed (red circle), calculated (solid black line) and the difference between observed and calculated (bottom blue curve) powder diffraction profiles are shown. Positions of all allowed Bragg reflections are indicated by vertical green tick marks. (c) View along [010] of the Fourier difference map of the skeleton structure $V_3O_8^{2-}$, where some negative residual peaks at (~0.25 0 ~0.15) were clearly detected. (d) Illustration of the crystal structure of $H_2V_3O_8$ in Space Group *Pnma*. [V(1)O_6] (yellow), [V(2)O_6] (green) octahedra and [V(3)O_5] (blue) square pyramids. Red spheres: oxygen. Small white spheres: hydrogen.

The crystal structure of $H_2V_3O_8$ can be described as a stacking of V_3O_8 layers along the *a*-axis, providing interlayer sites for lithium ions. Each V_3O_8 layer consists of corner- or edge-shared VO_6 octahedra and VO_5 square pyramids, forming a two-

dimensional slab in the *bc*-plane of the structure. Concerning the local structure around vanadium atoms, the structure is composed of double blocks of edge-sharing distorted $V(1)O_6$ and $V(2)O_6$ octahedra, which are corner-linked along the *c*-axis by edge-sharing up and down oriented pairs of $V(3)O_5$ pyramids which extend along the *b*-axis.[22, 36] Some authors[26, 37] instead describe the V(2) surrounding as square pyramids, because of the considerably larger bond length of V(2) to O1, 2.47 Å, when compared to other five much shorter bond lengths, in the range 1.61 - 2.06 Å, to other five oxygen atoms (O3 x 2, O4, O5, O6). As shown in Fig. 2d, two protons are bonded to O6 of one $V_3O_8^{2-}$ layer (V(2)-O6 bond length = 2.06 Å), forming a water molecule, oriented in such a way that each proton is hydrogen bonded to O5 (V(2)-O5 bond length = 1.61 Å) of different adjacent $V_3O_8^{2-}$ layers. Covalent O6-H bond lengths are 0.99 Å, with longer O5···H bond lengths of 1.90 Å characteristic of asymmetric hydrogen bonding. Structural water molecules are positioned at both sides of the V_3O_8 slab, where the water is directly bonded to $V(2)O_6$ or $V(2)O_5$ polyhedra (green color in Fig. 2d), hydrogen bonds connecting two neighboring V_3O_8 layers.

DFT calculations

Starting with the X-ray diffraction structure and according to NPD results, the arrangement of hydrogen atoms that displays the lowest energy in the $H_2V_3O_8$ structure (*Pnma* symmetry) is the one which places the two protons in O6, forming a water molecule oriented in such a way that both protons are hydrogen bonded to O5 atoms of contiguous layers.

If we generate a model with the space group symmetry $P2_12_12_1$, the reflection plane that forces hydrogen atoms to be equivalent disappears. In this model, we can analyze alternative models with independent orientations for hydrogen bonds and models with

one hydrogen attached to O6 and the second one bonded to another oxygen atom. Different models were generated for $H_2V_3O_8$, and geometry optimizations performed on each of them. Only one optimized configuration had lower energy than that obtained for the *Pnma* space group. In this model, two hydrogen atoms are attached to O6, but their orientation is not symmetric. While one proton forms a hydrogen bond with an O5 (as observed by neutron diffraction), the other one forms a hydrogen bond with O8 oxygen (Fig. 3). The energy of this configuration is only 0.07 eV/f.u. lower than that obtained with the two hydrogen atoms bonded to O5. The energy difference between both configurations is small and orientations not very different, so a dynamic exchange between these two configurations could be proposed. The positions of the V and O atoms in this model display small deviations with respect to the *Pnma* symmetry.

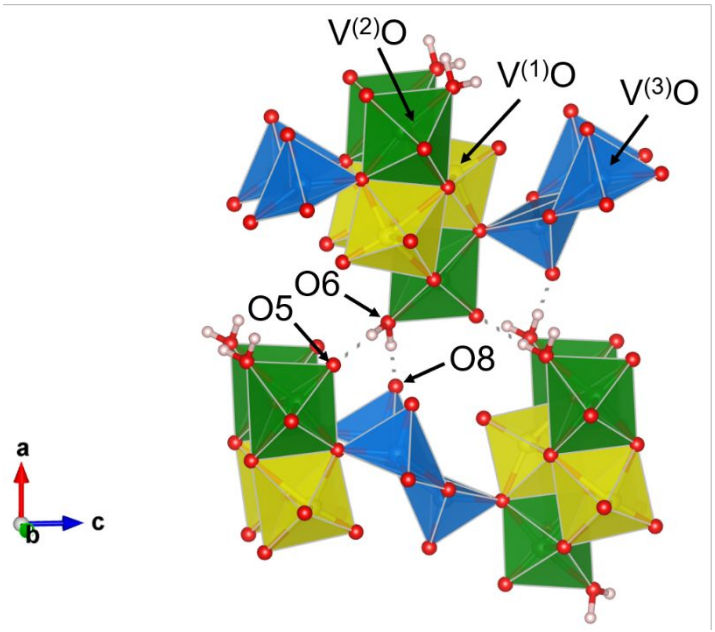

Fig. 3: Detail of the DFT optimized structure of $H_2V_3O_8$ in Space Group $P2_12_12_1$. $[V(1)O_6]$ (yellow), $[V(2)O_6]$ (green) octahedra and $[V(3)O_5]$ (blue) square pyramids. Red spheres: oxygen. Small white spheres: hydrogen.

^{1}H (I= 1/2) MAS NMR spectroscopy

In the ^{1}H MAS NMR spectrum of the $H_2V_3O_8$ sample (Fig. 4), the deconvolution displayed six components; three external ones at ~ 40, 30 and -20 ppm displaying very low intensity and three others in the preponderant central region, fitted with three components (4.8, 5.5 and 7.7 ppm), that were ascribed to water molecules. The detection of two bands at ~ 5 ppm with different linewidth suggest the existence of local reorientations of water with different exchange rate. The shift of the water band to 7.7 ppm underlines the presence of stronger hydrogen bonds of water molecules with neighboring polyhedra.

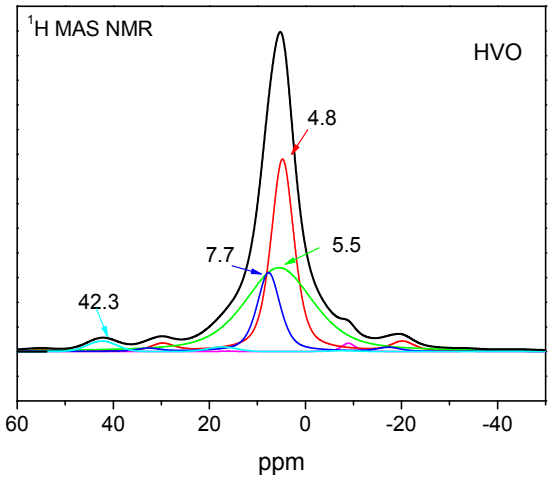

Fig. 4. The central part of the ^{1}H MAS NMR spectrum of the microwave assisted hydrothermal $H_2V_3O_8$ sample.

The shift of small bands at 40, 30 and -20 ppm, indicate the presence of other minor secondary phases, where protons are submitted to bigger interactions. Parameters deduced from the deconvolution of ^{1}H MAS NMR spectra are given in Figure 4 and Table 1.

Magnetic measurements

The temperature dependence of the magnetic susceptibility for $H_2V_3O_8$ obtained by the microwave-assisted hydrothermal route is shown in Fig. 5, from which a decrease in the susceptibility value with increasing temperature was detected, with no differences between ZFC and FC curves.

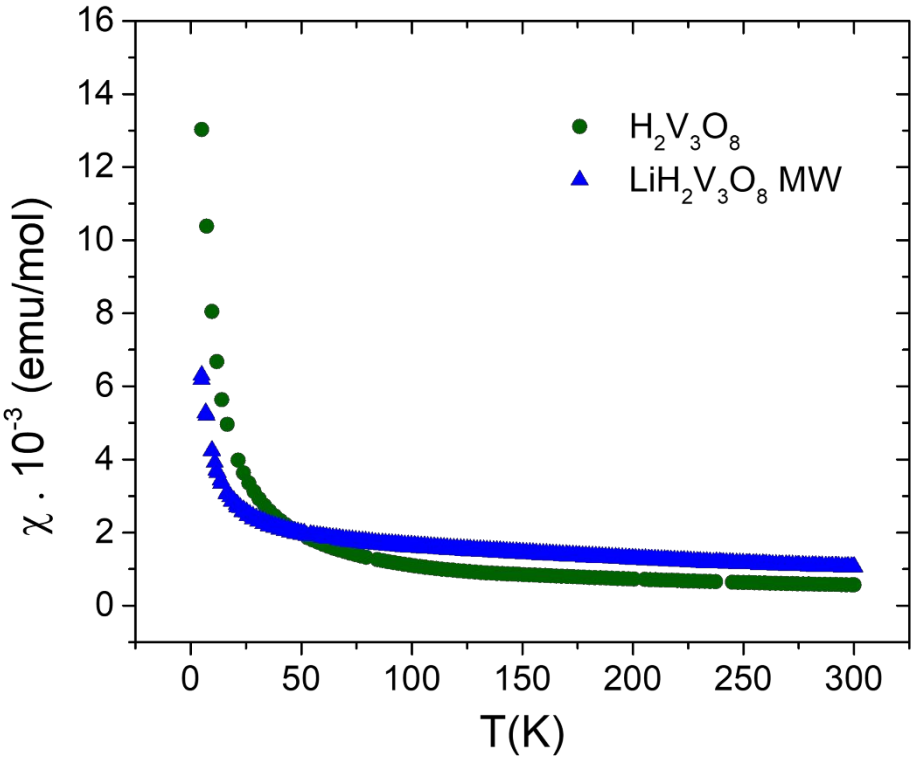

Fig. 5. Temperature dependence of the magnetic susceptibility χ of $H_2V_3O_8$ (green circles) and $LiH_2V_3O_8$ (blue triangles) at 0.1 T in ZFC and FC experiments.

The magnetic behavior of this material, which was previously described by Hellmann et al., corresponds to a paramagnetic regime.[49] By applying the Curie–Weiss-fit to the data from room temperature to ≈ 130 K, an effective moment (μ) of 1.41 μB is determined. This value is in good agreement with the predicted theoretical effective moment of 1.73 μB, considering an atom of V^{4+} (d^1) and 2 atoms of V^{5+} (d^0) in $H_2V_3O_8$. A negative Curie-

Weiss temperature (θ) of -144 K is obtained, which is indicative of antiferromagnetic interactions. Fig. S2 presents the magnetization vs applied field plots at 5 K and 300 K for $H_2V_3O_8$ (top). There is no evidence of hysteresis loop, so there is not any weak ferromagnetic signal that could contribute to the magnetism of the samples.

Characterization of the lithiated $LiH_2V_3O_8$ phase

Structure determination of $LiH_2V_3O_8$

The crystal structure of $LiH_2V_3O_8$ was determined here for the first time. The crystal structure analysis of the lithium intercalated $Li_xH_2V_3O_8$ (x = 1) phase was first performed using the synchrotron X-ray diffraction data. The synchrotron diffraction pattern of $LiH_2V_3O_8$ was successfully indexed with space group *Pnma* (#62). Refined lattice parameters were a = 16.552(1) Å, b = 3.6684(3) Å, c = 9.3469(9) Å, Vol = 567.54 $Å^3$. As X-ray data do not permit to accurately determine Li and H positions, the lithium sites in $LiH_2V_3O_8$ were deduced from BVS isosurfaces obtained from the structural model refined with X-ray (synchrotron) data, in which the H atoms were arranged as in non-lithiated $H_2V_3O_8$, i.e., each proton is hydrogen bonded to O5. BVS suggested two possible lithium positions at (~0.27 0.25 ~0.35) and (~0.32 0.25 ~0.32). Parallel to this, the location of the hydrogen atoms in $LiH_2V_3O_8$ was addressed by difference Fourier synthesis deduced from powder ND data collected at 300K using a structural model in which H and Li were not included. For refinements with powder neutron diffraction data, positions and thermal factors of vanadium and oxygen atoms were taken from those deduced from synchrotron diffraction data. Fig. 6a shows the map of the y = 0 (xz plane) section. Some negative residual density associated with H atoms was detected at 8d position (~0.23 0 ~0.12). Subsequent difference Fourier synthesis after introducing the H atoms in the structural model yielded a neutron-density map (Figure 6b) that displays an

additional negative neutron scattering peak for Li at 4c position in the xz section at coordinates (~0.35 0.25 ~0.32). This negative density peak matches with the second one deduced from BVS isosurfaces for Li^+ ions. Synchrotron X-ray and neutron diffraction patterns and differences between observed and calculated data for $LiH_2V_3O_8$ are shown in Fig. 6c and d, respectively.

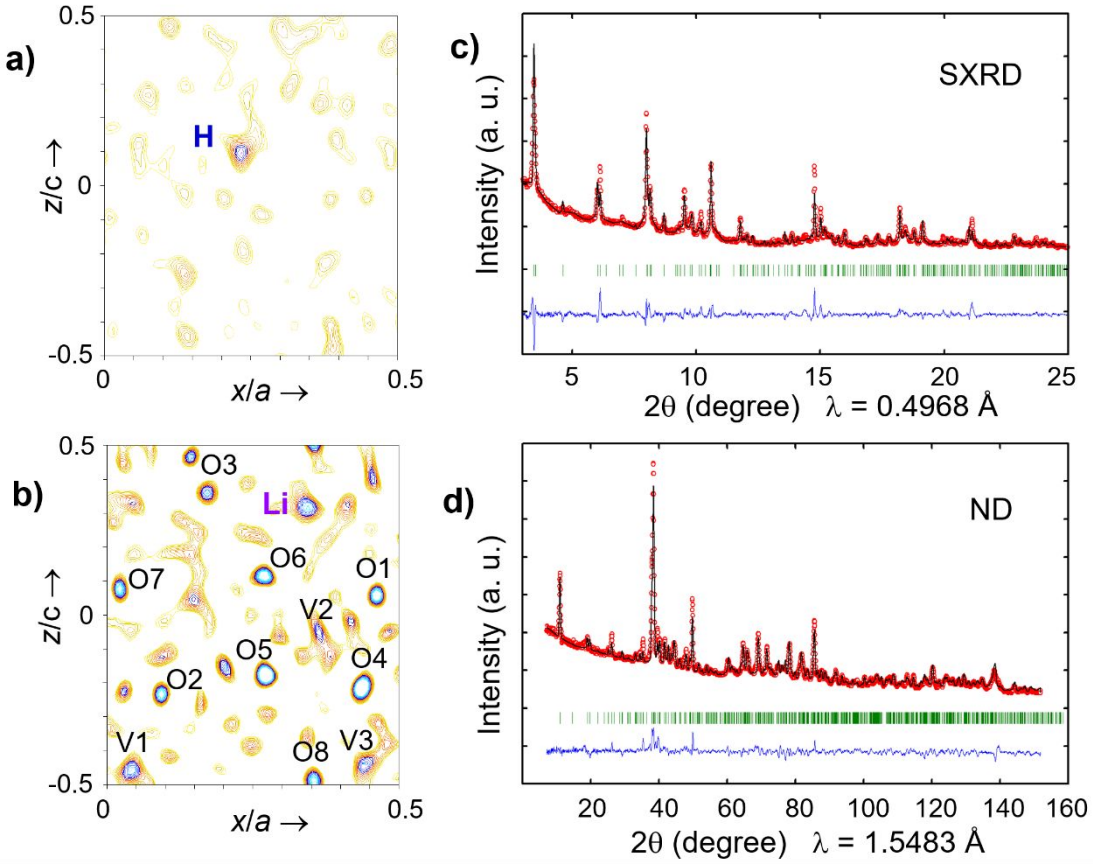

Fig. 6. (a) (010) view of the Fourier difference map for $LiH_2V_3O_8$ from neutron diffraction data using only the heavy atom structure of $V_3O_8^{2-}$. The negative residual density at (~0.23 0 ~0.12) corresponds to the H site. (b) View on the same (010) plane of the Fourier difference map for $LiH_2V_3O_8$ with the $H_2V_3O_8$ structural model after positioning H atoms. The negative residual density at (~0.35 0.25 ~0.32) corresponds to

the Li site. The powder X-ray (synchrotron) (c) and neutron (d) Rietveld refinement profile for $LiH_2V_3O_8$ at 25ºC. Observed (red circle), calculated (solid black line) and the difference between observed and calculated (bottom blue curve) powder diffraction profiles are shown. Positions of all allowed Bragg reflections are indicated by vertical green tick marks.

The crystal structure of $LiH_2V_3O_8$ is presented in Fig. 7a. Crystal data deduced from structure refinements, together with atom parameters and interatomic distances are summarized in Tables S3 and S4, respectively.

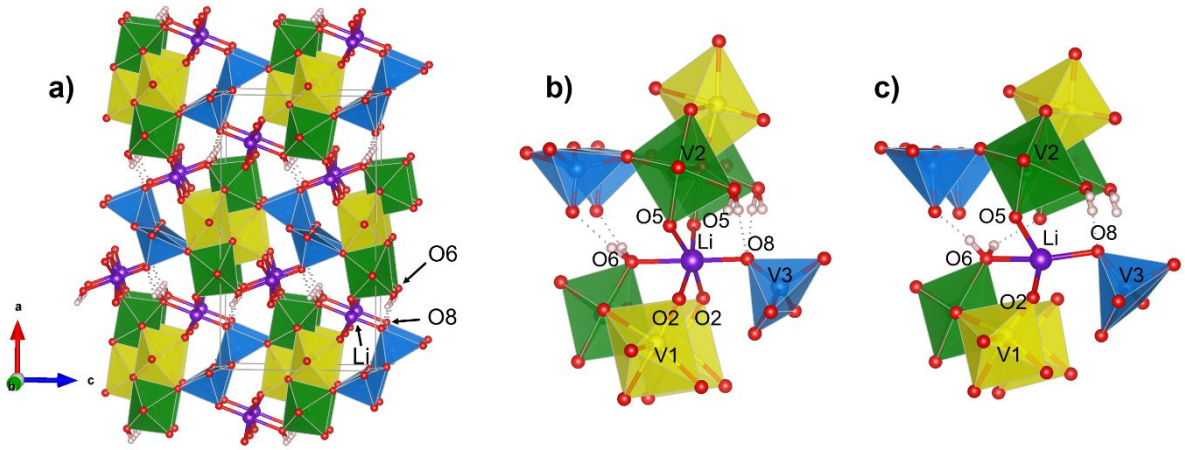

Fig. 7. (a) The crystal structure of $LiH_2V_3O_8$ (Space Group *Pnma*) formed by $[V(1)O_6]$ (yellow), $[V(2)O_6]$ (green) octahedra and $[V(3)O_5]$ (blue) square pyramids. Red spheres: oxygen. Small white spheres: hydrogen. Li-oxygen bonds are drawn with Li denoted by the purple spheres. Local environment around inserted lithium obtained from ND (b) and DFT (c). Space groups used were *Pnma* and $P2_12_12_1$, respectively.

It can be clearly seen that inserted Li ions are located in cavity sites of the interlayer space between V_3O_8 layers. Fig. 7b shows the local environment of the intercalated Li

atom, bonded to six oxygen atoms (O6, O8 and two O2 and O5 atoms) with interatomic Li−O distances ~ 2.13, 1.94, 2.25 and 2.23 Å, respectively. It forms distorted LiO_6 octahedra with the Li atom at its center. As for $H_2V_3O_8$, structural water molecules are positioned at both sides of the V_3O_8 slab, with water molecules directly bonded to V(2) atoms (green color in Fig. 7a), and hydrogen bonded to two neighboring V_3O_8 layers. In both $H_2V_3O_8$ and $LiH_2V_3O_8$, two hydrogen atoms are attached to O6 with a covalent O6-H bond length of 0.93 Å. While the protons form hydrogen bonds with O5 in $H_2V_3O_8$, the protons in $LiH_2V_3O_8$ form hydrogen bonds with O8, with longer O8···H bond lengths of 2.0 Å. This is nicely illustrated in Fig. S3, where the unit cell of $H_2V_3O_8$ before and after lithiation is viewed along [010]. The switch of the hydrogen bond from O5 to O8 increases considerably Li^+- H^+ distances (from 2.04 Å if bonded to O5 to 2.77 Å bonded to O8), thereby minimizing Li^+- H^+ repulsions.

DFT results of the lithiated phase

For the lithiated $LiH_2V_3O_8$ compound, geometry optimizations were carried out in two models deduced from the X-ray (synchrotron) diffraction data. In these two models, the water molecule was in the same orientation than in the pristine sample, and tentative positions for Li atoms deduced with BVS were considered. A first study was addressed to analyze the most favorable position for the lithium atom in the *Pnma* model, considering hydrogen atoms as part of a water molecule located at O6 and forming hydrogen bonds with two neighbor O5 atoms. In one of the models, lithium atoms are located at distances shorter than 2.3 Å towards one O8, two O5 and one O3 (Fig. S4a). While the two protons of the water molecule are located approximately at 2.2 Å from the Li ion. In the second model, lithium atoms are located at shorter distances than 2.3 Å from one O8 and one O6 (Fig. S4b). The two hydrogen atoms of the H_2O molecule are only

1.7 Å away from Li ions. Both models converge to the same structure when performing geometry optimizations. The main conclusion refers to the modification of the orientation of the water molecule, with its hydrogen atoms forming hydrogen bonds with O8 instead of O5. The lithium atom is located near the starting position of model 2. The final coordination of the lithium is with one O6 and one O8 atom at distances less than 2.2 Å and with two O2 atoms at approximate 2.2 Å. The resulting structure is very similar to that obtained with neutron diffraction (Fig. 7b), but in this latter case, it is obtained with X-ray (synchrotron) diffraction and DFT optimization.

In a second set of optimizations, an attempt was made to determine the most favorable allocation of hydrogen atoms. In this case, models were built placing the lithium atom in the most favorable position deduced previously. To relax structural constraints, the symmetry plane, which makes the two hydrogen atoms equivalent, was eliminated (space group $P2_12_12_1$). In these models, hydrogen atoms can be placed in pairs or individually on O6, O5 and O8 atoms. The configuration with the lowest energy, at which four of tested models converge, has the same structural features described in previous optimizations. In absence of the symmetry plane, the main difference is associated with a higher freedom for hydrogen and lithium atoms allocation. (Fig. 7c). In this configuration, the Li atom is slightly displaced from the lost symmetry plane, giving the following Li-O distances: O2: 1.97 Å; O8: 2.04 Å; O5: 2.10 Å and O6: 2.14 Å. The five shortest Li-V distances are: V1: 3.16 Å; V1: 3.64 Å; V2: 3.36 Å; V2: 3.77 Å and V3: 3.23 Å. The hydrogen atoms form a water molecule in O6, but the orientation is a bit tilted, giving a strong hydrogen bond to one O8 and a weak hydrogen bond to one O5. This configuration is only slightly more stable than that of *Pnma*, and an exchange between these configurations can be proposed. A molecular dynamics simulation to study this exchange can be found in the Supporting Information (Note 1). Configurations with

protons on different oxygen atoms are more unstable than the lowest energy one described above. The increase of energy in some of these configurations is only around 0.45 eV per split water molecule.

Evolution of crystal structure during cycling

The variation of unit cell parameters, volume, and V-O bond lengths, determined from Rietveld refinements with SXRD and ND data (x=0 and 1.0), are presented in Fig. S5. Upon lithiation, the unit cell parameters change anisotropically (Fig. S5a). The *a*-axis decreases by 1.8% (16.8603 to 16.5520 Å), whereas the *b*-axis and *c*-axis increase by 0.9% (3.6340 to 3.6684 Å) and 0.2% (9.3327 to 9.3469 Å), respectively. Overall, the unit cell volume decreases slightly by 0.7% (571.82 to 567.54 $Å^3$). The small change in volume contributes to the excellent cycle stability detected in this solid solution range. It is interesting to note that the increase detected in both *b* and *c* parameters agrees with the increment of ionic radii of vanadium produced upon Li insertion (V^{5+} to V^{4+} reduction), previously deduced by EELS technique.[22] The opposite variation of *a* parameter is remarkable and is thought to be related to a change in the interlayer space, as observed upon magnesium intercalation into $H_2V_3O_8$ that slightly affects the arrangement of contiguous layers[26], an increase of interlayer attraction forces or changes on the Li^+ ion disposition in the interlayer space.[50]

The reduction in vanadium oxidation state leads to a large increment in average V−O distances (Figure S5b): V1−O (from 1.941 to 2.017 Å), V2−O (1.901 to 1.913 Å for pyramidal $[V(2)O_5]$ coordination, and V3−O (1.830 to 1.840 Å). When considering octahedral coordination for V(2), the apparent decrease of average V-O distances is connected with the considerable shortening of the V(2)-O1 bond length upon lithiation from 2.473 Å in $H_2V_3O_8$ to 2.18 Å in $LiH_2V_3O_8$. The more regular octahedral surrounding

of V(2) in $LiH_2V_3O_8$ is in agreement with its reduction (to V^{4+}) upon lithiation, as deduced from bond valence sum calculations. The sum of bond valences for V(2), close to +5 in $H_2V_3O_8$, was found to decrease to +4.1 in $LiH_2V_3O_8$.

Magnetic measurements

As for $H_2V_3O_8$, the magnetic behavior of $LiH_2V_3O_8$ is described as a paramagnetic system (Fig. 5).[49] The reduction of the overall oxidation state of vanadium in the lithiated sample (confirmed by EELS in the preceding work[22]) affects considerably to the magnetism of the material. From the Curie-Weiss fit of data, from RT to 35 K, an effective moment of μ=2.31 μB is found. This result is in good agreement with the theoretical effective moment of 2.45 μB, taking into account the presence of 2 atoms of V^{4+} (d^1) and 1 atom of V^{5+} (d^0). Theoretical studies of Sarkar et al.[23] are consistent with this result. In their work, they suggest that in lithiated $H_2V_3O_8$, although oxygen gains a higher amount of the transferred charge, strong covalency results from the molecular orbital formation, which produces a notable increase of the magnetic moment. Here, the negative Curie-Weiss temperature is -269 K. Not any weak ferromagnetic contribution to magnetism of the sample is evidenced from magnetization vs applied field plots performed at 5 K and 300 K (Fig. S2).

Bond Valence Sum Difference Maps (BVS-DMs) Calculation

The BVS-DMs are generally used to find plausible locations for intercalated ions and to probe ion conduction pathways in inorganic materials. Thus, a three-dimensional (3D) BVS-DM calculation was performed using the crystallographic information derived from the structural refinements (Table S3). Fig. 8 shows BVS-DM isosurfaces at $|\Delta v| = 0.2$ valence units (v.u.) for Li ions. The positions deduced here are not far from those deduced

during structural refinements. The most possible lithium-ion diffusion pathways are noted in the interlayer space, providing additional support for the electrochemical lithium intercalation into $H_2V_3O_8$. Li ions are allocated between two contiguous water molecules, increasing Li-H interactions. The Li motion will decrease electrostatic repulsions.

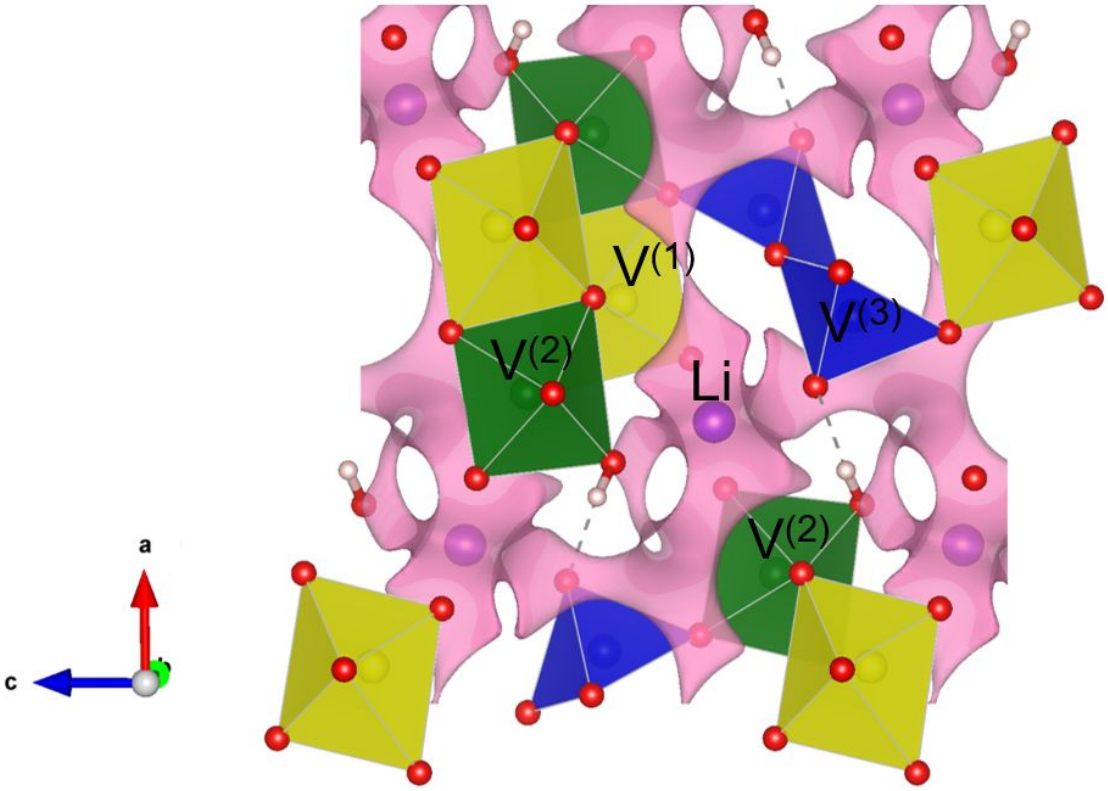

Fig. 8. 3D bond valence difference map isosurfaces (light purple) for $LiH_2V_3O_8$ with the isosurfaces of |0.2| valence units (oxygen atoms: red spheres; $V(1)O_6$ octahedra: yellow; $V(2)O_5$ square pyramids or $V(2)O_6$ octahedra: green; $V(3)O_5$ square pyramids: blue). Purple spheres: Li; red spheres: O; small white spheres: H.

MAS-NMR spectroscopy of lithiated samples

To assess the lithium allocation during lithiation ($0 < x < 1$), two samples with nominal lithium contents $x = 0.5$ and 1.0 were analyzed. Significant differences were observed in

^{1}H spectra of pristine and lithiated samples. However, smaller changes were detected in ^{1}H and ^{7}Li NMR spectra as lithiation progresses.

^{51}V (I= 7/2) MAS NMR

In Fig. 9, ^{51}V MAS-NMR spectra of pristine and lithiated samples are referred to the V_2O_5 compound (bottom spectrum), where signals are not affected by paramagnetic interactions. In agreement with the reported structure of V_2O_5, ^{51}V MAS-NMR spectra display a single component at δ_0 = -610 ppm, with constants C_Q = 0.8 MHz and η = 0.04.[51]

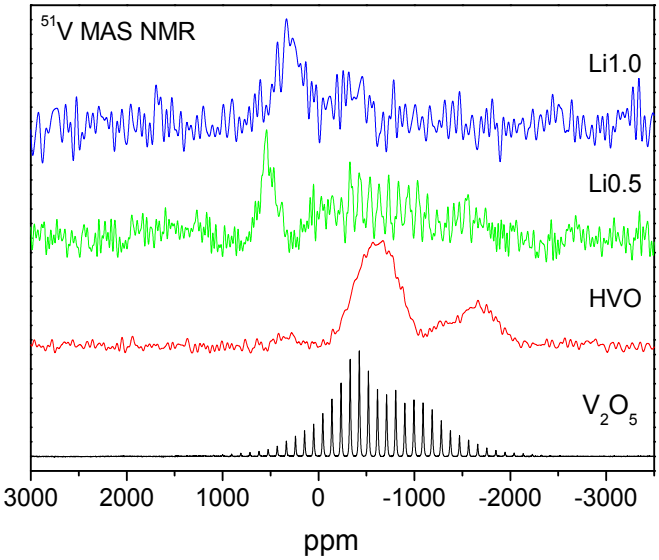

Fig. 9. ^{51}V MAS NMR spectra of starting (HVO) and lithiated (Li0.5, Li1.0) samples.

In $H_2V_3O_8$ (HVO), the mean oxidation state of vanadium is 4.67+. From this fact, the intense signals detected at -500 and -1500 ppm (Fig. 9, HVO) have been ascribed to penta and hexacoordinated V^{5+} and the smaller band at +500 ppm to V^{4+} ions. Moreover, the band at -1500 ppm of $H_2V_3O_8$ should correspond to $V(2)^{5+}$ coordinated to water molecules, because the progressive reduction of V(2) species eliminates this component

(Fig. 10, Li0.5 and Li1.0). Finally, the band at +500 ppm has been mainly ascribed to $V(3)^{5+}$ ions of the HVO sample. The absence of spinning side bands in pristine and lithiated samples underlines the presence of heterogeneous paramagnetic interactions that enlarge main components.

In $Li_{0.5}H_2V_3O_8$, the modulated signal at -600 ppm corresponds to the presence of some segregated V_2O_5 (Fig. 9). In ^{51}V MAS-NMR spectra of lithiated samples, the most intense signal corresponds to V^{4+} (V1 and V2 sites). However, the band detected at -500 ppm correspond to $V(3)^{5+}$ species (Fig. 9, Li0.5 and Li1.0). As lithiation progresses, the amount of V^{4+} increases at the expense of V^{5+}, confirming the above assignments (Fig. 9). The position and broadening of components are affected by the amount and distribution of V^{4+} cations.

^{1}H (I=1/2) MAS NMR

^{1}H MAS-NMR spectra of lithiated samples (Fig. 10b and Table 1), display an intense component at 0 ppm, besides a small broad signal at 5 ppm. The component at 0 ppm could be ascribed to OH groups; however, the bonding of water to $V(2)^{4+}$ could shift the corresponding band towards negative values. In this case, the reorientation of water molecules could decrease the linewidth of this band. On these bases, water molecules bonded to V^{4+} or V^{5+} cations could produce detected 0 and 5 ppm components in $Li_{0.5}H_2V_3O_8$ sample. However, in $Li_1H_2V_3O_8$, the total reduction of V(2) ions should produce the elimination of the 5 ppm band, what was not observed experimentally.

To explain the results described, the 0 ppm component could be ascribed to OH groups, created by the water splitting to reduce electrostatic Li^+-H^+ repulsions. When Li changes its position, water could be again formed. On these bases, local motion of lithium could explain the presence of 0 and 5 ppm bands. As the lithiation degree progresses,

paramagnetic interactions increase, enlarging the region occupied by spinning side bands patterns. The results of spectra deconvolution are summarized in Figure S6.

Table 1: ^{1}H MAS-NMR parameters of pristine $H_2V_3O_8$ (HVO) and Li inserted samples $Li_{0.5}H_2V_3O_8$ (Li05HVO) and $LiH_2V_3O_8$ (Li1HVO). CSA: chemical shift anisotropy

HVO (ppm)	42.34	7.66	5.49	4.76	
CSA (kHz)/eta	50/0.8	20/0	-	20/0	
%	3.8	15.2	43.5	36.5	
Li05HVO (ppm)	---	7.92	---	4.84	0.23/0.08/0.01
CSA/eta	---	50/0	---	50/0	50/0
%	---	5.9	---	13.4	80.7
Li1HVO (ppm)	---	8.85	5.72	---	-0.76,-0.38,-0.08
CSA/eta	---	60/1	60/0.5	---	50/0, 70/0, 70/1
%	---	14.9	18.5	---	66.6

^{1}H NMR spectra do not change significantly with temperature, suggesting that water molecules maintain their structural position, preserving interactions with neighboring layers.

^{7}Li (I=3/2) MAS NMR

In Fig. 10a, ^{7}Li MAS-NMR spectra of lithiated samples are formed by an intense component ~ -25 ppm, surrounded by the corresponding spinning sidebands. The results of spectra deconvolution are summarized in Figure S7 and Tables S5 and S6.

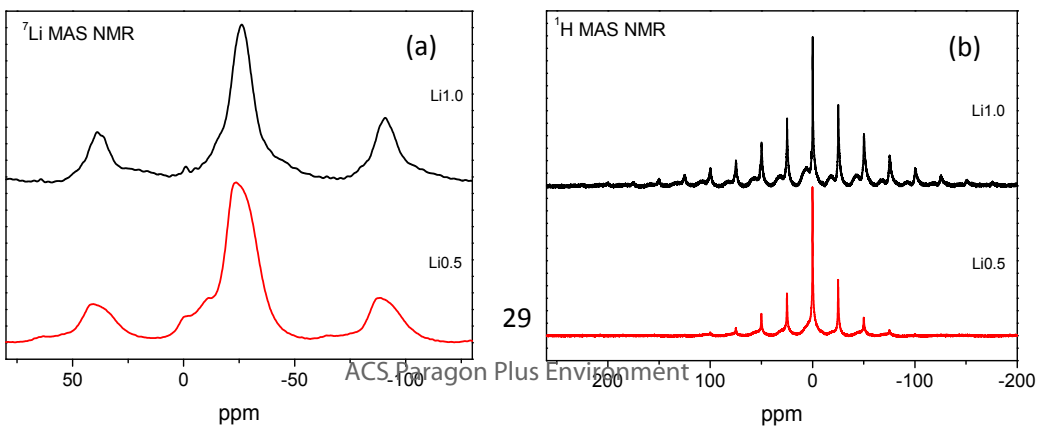

Fig. 10. ^{7}Li (a) and ^{1}H (b) MAS NMR spectra of $Li_{0.5}H_2V_3O_8$ and $Li_{1.0}H_2V_3O_8$. In all cases, spinning side bands of samples are illustrated.

In general, the higher the number of V^{4+} cations arranged around Li ions, the more the NMR line shifts towards negative positions. On these bases, bands detected at ~ -10 ppm correspond to lithium surrounded by 2 $V(1)^{4+}$ (Fig. 7b), the band located at -23 ppm is ascribed to $2V(1)^{4+}1V(2)^{4+}$ and the component at -30 ppm to $2V(1)^{4+}2V(2)^{4+}$. Finally, the component at -43 ppm is assigned to $2V(1)^{4+}3V(2)^{4+}$ environments.

The structural refinement of lithiated samples indicates that mean Li-H distances are near 2.8 Å, favoring the polarization transfer in cross polarization experiments. Cross-polarization (CP) experiments performed in ^{7}Li MAS-NMR signals showed that the -30 ppm signal corresponds to Li species located at longer distances from water protons than those of -23 ppm. In $LiH_2V_3O_8$ exchange motions between neighboring sites increase, averaging chemical shift values and decreasing the efficiency on CP experiments.

In two lithiated samples, spinning sideband patterns have been used to deduce quadrupolar constants. In the case of the $Li_{0.5}H_2V_3O_8$ sample, C_Q values are between 30 and 70 kHz, and η values near 0 (axial symmetry). In the case of $Li_{1.0}H_2V_3O_8$, C_Q values are between 40 and 80 kHz, and η values near 0.5. This observation suggests that inserted lithium occupies more distorted sites when lithiation progresses.

Temperature dependence of ^{7}Li NMR spectra

The temperature dependence of ^{7}Li MAS-NMR spectra was analyzed in lithiated samples. The linear shift detected with inverse temperature (Fig. 11 and 12), illustrates the linear dependence of paramagnetic V^{4+} moments with temperature. In the two lithiated samples,

signals detected at -5 and -10 ppm correspond to Li ions subjected to small paramagnetic interactions (Li atoms located far from V^{4+} cations).

In $Li_{0.5}H_2V_3O_8$ (Fig. 11a), two signals detected between -20 and -30 ppm have been ascribed to lithium ions (a single Li site) located near three and four V^{4+} cations. These components shift with temperature and coalesce at ~325 K, giving a narrower component at ~ -20 ppm (Fig. 12a). This observation has been associated with local exchange motions between Li ions located at these two sites. Upon cooling, initial positions and spectra were recovered (Fig. 11a).

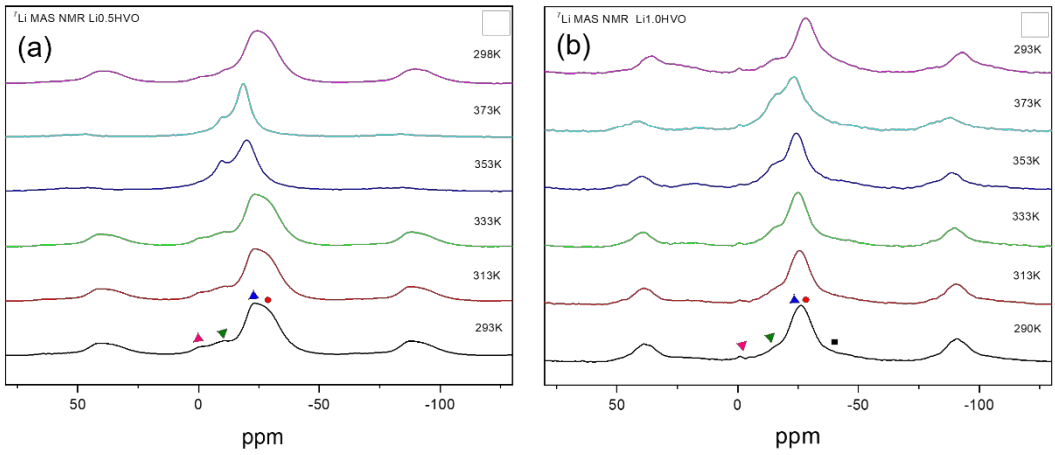

Fig. 11: Temperature dependence of ^7Li NMR spectra of (a) $Li_{0.5}H_2V_3O_8$ and (b) $Li_{1.0}H_2V_3O_8$ samples. Symbols designated for the different lithium signals are those used in Fig. 12.

The temperature dependence of ^7Li MAS-NMR spectra of the $Li_{1.0}H_2V_3O_8$ sample (Fig. 11b) is considerably different. Following the previous assignment, Li components located near -20/-30 ppm correspond to Li species located near three and four V^{4+} cations, and the broad one at ~ -40 ppm to Li ions located at $2V(1)^{4+}3V(2)^{4+}$ environments. In general, shifted lines change their position more strongly with temperature than non-

shifted ones, suggesting that lithium species located near V^{4+} cations display higher mobility. The position of -30 and -40 ppm components departs abruptly from expected values at 350K, suggesting the displacement of Li to new structural sites (Fig. 12b).

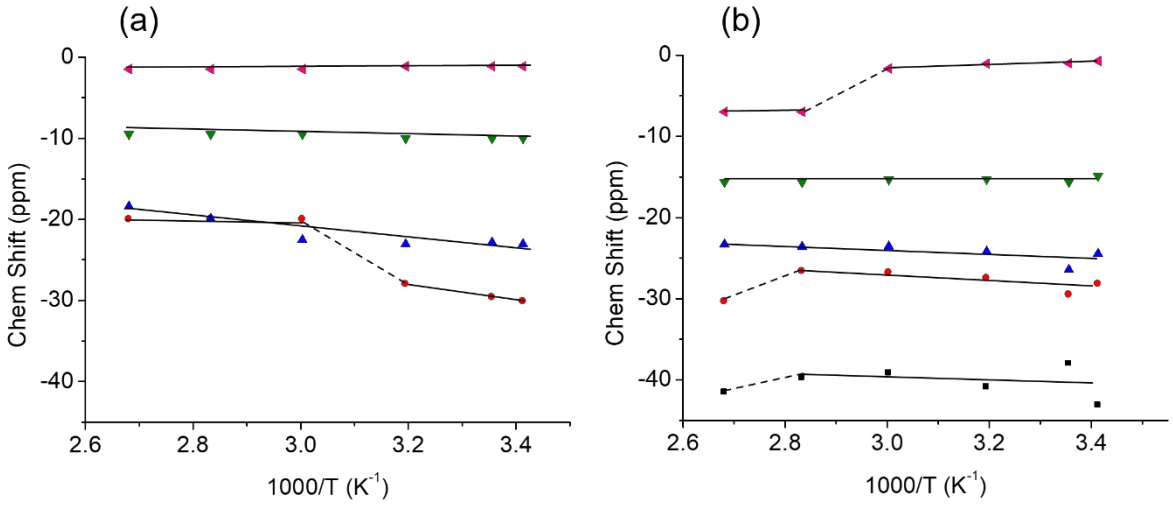

Fig. 12. Inverse temperature dependence of Li components in (a) $Li_{0.5}H_2V_3O_8$ and (b) $Li_{1.0}H_2V_3O_8$ samples.

The analysis of unit cell parameters measured before and after lithiation indicates that *a* parameter is considerably reduced, suggesting that separation between contiguous $H_2V_3O_8$ layers decreases as a consequence of Li insertion, hindering slightly the Li motion.

On the other hand, CP experiments performed in lithiated samples have shown, in agreement with structural refinements, that water protons are near Li atoms (~ 2.5 Å), promoting the Li motion. In all cases, Li mobility is considerably higher than that detected for protons, indicating that protons participate to the stabilization of the $H_2V_3O_8$ network. Finally, some reorientation of water molecules can be produced when Li ions move.

Conclusions

We evaluate the structural evolution of $H_2V_3O_8$ upon Li intercalation occurring in the high voltage range 3.5 - 2.75 V vs. Li^+/Li. We present for the first time an accurate description of the crystal structures of pristine and lithiated $H_2V_3O_8$, including the light elements hydrogen and lithium, by means of a combination of high-resolution diffraction techniques (ND, SXRD). Lithiation leads to a shrinkage of the interlayer distance, caused by the reorientation of structural water upon lithium intercalation, as evidenced from both diffraction techniques and DFT calculations. This is in line with the shrinkage of the interlayer spacing observed upon Mg intercalation[26], but opposite to the effect observed upon sodiation in $H_2V_3O_8$, where an enlargement of the interlayer spacing is observed[34]. The structural water plays a central role in stabilizing the V-O network, in which extended water hydrogen bonding mitigate the volume changes of vanadium layers during lithium intercalation, key factor in the outstanding electrochemical properties of $H_2V_3O_8$ as high-capacity cathode in LIBs. In the electrochemical window investigated, the preferential reduction of $V(2)^{5+}$ cations was produced, favoring the onset of weak antiferromagnetic interactions that enables further DFT and NMR studies. Further investigations of the lithium-proton distribution around vanadium ions by means of NMR show that the mobility of lithium is favored by electrostatic repulsion between lithium and water protons. DFT and NMR reveal the (temporary) formation of OH groups by splitting water to reduce electrostatic Li^+-H^+ repulsions, and water could be formed back as lithium moves further. At increasing temperatures, local motions are produced; however more extended motions were not detected.

On one hand, the new insights gained in this article into the crystal structure of $H_2V_3O_8$, employing water-metal and hydrogen bonding opens new opportunities to discover new

high-energy hydrated oxide materials for LIBs and other MIBs. On the other hand, future *in operando* studies on the intercalation mechanism in $H_2V_3O_8$ might be of great interest to elucidate the reasons for its ability to intercalate other guest ions (Na^+, K^+, Mg^{2+} or Zn^{2+}).

Supporting Information

The Supporting Information is available free of charge on the ACS Publications website at DOI:

SEM/TEM images, magnetization plots, hydrogen bonding in $H_2V_3O_8$ and $LiH_2V_3O_8$, conformations of Li and H atoms for DFT optimization, evolution of unit cell parameters in $Li_xH_2V_3O_8$, 1H and 7Li MAS NMR spectra, crystallographic data for $H_2V_3O_8$ and $LiH_2V_3O_8$, ^{7}Li NMR deconvolutions of $Li_{0.5}H_2V_3O_8$ and $Li_1H_2V_3O_8$ at different temperatures, note to Molecular Dynamic study of $LiH_2V_3O_8$.

Author Information

Corresponding Authors

* (A.K.) Email: akuhn@ceu.es

Conflicts of interest

There are no conflicts of interest to declare.

Acknowledgements

We thank Agencia Estatal de Investigación (AEI)/Fondo Europeo de Desarrollo Regional (FEDER/UE) for funding the project MAT2016-78632-C4-R1,2 and PID2019-

106662RB-C41,2. The regional government of Comunidad de Madrid is acknowledged for funding the project MATERYENER3CM S2013/MIT-2753 and PR65/19-22459. The synchrotron diffraction experiments at ESRF were funded through the proposal with reference 25-01-857. We are indebted to Dr. A.M. Arévalo-López for help and support during SXRD data collection.

In Memoriam of our esteemed colleague and friend Emilio Morán, chair professor of Inorganic Chemistry at Universidad Complutense de Madrid, who synthesized for the first time $H_2V_3O_8$ by means of green chemistry microwave-assisted techniques.

References

(1) Legagneur V.; Le Gal La Salle, A.; Verbaere, A.; Piffard Y.; Guyomard D. Lithium Insertion/deinsertion Properties of New Layered Vanadium Oxides Obtained by Oxidation of the Precursor $H_2V_3O_8$. *Electrochim. Acta* **2002**, *47*, 1153-1161.

(2) Whittingham M. S.; Song Y. N.; Lutta S.; Zavalij P. Y.; Chernova N. A. Some Transition Metal (oxy)phosphates and Vanadium Oxides for Lithium Batteries. *J. Mater. Chem.* **2005**, *15*, 3362-3379.

(3) Chernova N.A.; Roppolo M. A.; Dillon C; Whittingham M.S. Layered Vanadium and Molybdenum Oxides: Batteries and Electrochromics. *J. Mater. Chem.* **2009**, *19*, 2526-2552.

(4) Pang H. C.; Cheng P.; Yang H. B.; Lu J. L.; Guo C. X.; Ning G. L.; Li C. M. Template-free bottom-up Synthesis of Yolk–shell Vanadium Oxide as High Performance Cathode for Lithium Ion Batteries *Chem. Commun.* **2013**, *49*, 1536-1538.

(5) Pan A.; Zhang J. G.; Nie Z.; Cao G.; Arey B. W.; Li G., Liang S. Q.; Liu J. Facile Synthesized Nanorod Structured Vanadium Pentoxide for High-rate Lithium Batteries. *J. Mater. Chem.* **2010**, *20*, 9193-9199.

(6) Yu J.; Yu J.C.; Ho W.; Wu L.; Wang X. A Simple and General Method for the Synthesis of Multicomponent $Na_2V_6O_{16}\cdot 3H_2O$ Single-Crystal Nanobelts. *J. Am. Chem. Soc.* **2004**, *126*, 3422-3423.

(7) Li G.-C.; Pang S.-P.; Wang Z.-B.; Peng H.-R.; Zhang Z.-K. Synthesis of $H_2V_3O_8$ Single-Crystal Nanobelts. *Eur. J. Inorg. Chem.* **2005**, *11*, 2060-2063.

(8) Lui J.; Wang X.; Peng Q.; Li Y. Vanadium Pentoxide Nanobelts: Highly Selective and Stable Ethanol Sensor Materials. *Adv. Mater.* **2005**, *17*,764-767.

(9) Wang Z. L.; Xu D.; Wang L. M.; Zhang X. B. Facile and Low-Cost Synthesis of Large-Area Pure V_2O_5 Nanosheets for High-Capacity and High-Rate Lithium Storage over a Wide Temperature Range. *ChemPlusChem* **2012**, *77*, 124- 128.

(10) Mai L.; Xu X.; Xu L.; Han C.; Luo Y. Vanadium Oxide Nanowires for Li-ion Batteries. *J. Mater. Res.* **2011**, *26*, 2175-2185.

(11) An Q.; Sheng J.; Xu X.; Wei Q.; Zhu Y.; Han C.; Niu C.; Mai L. Ultralong $H_2V_3O_8$ Nanowire Bundles as a Promising Cathode for Lithium Batteries. *New J. Chem.* **2014**, *38*, 2075-2080.

(12) O'Dwyer C.; Navas D.; Lavayen V.; Benavente E.; Santa Ana M.A.; González G.; Newcomb S.B.; Sotomayor Torres C.M. Nano-Urchin: The Formation and Structure of High-Density Spherical Clusters of Vanadium Oxide Nanotubes. *Chem. Mater.* **2006**, *18*, 3016-3022.

(13) Xu H.; He W.; Wang H.; Yan H. Solvothermal Synthesis of $K_2V_3O_8$ Nanorods. *J. Cryst. Growth* **2004**, *260*, 447-450.

(14) Wu X.; Tao Y.; Dong L.; Hong J. Synthesis and Characterization of Self-assembling $(NH_4)_{0.5}V_2O_5$ Nanowires. *J. Mater. Chem.* **2004**, *14*, 901-904.

(15) Lutta S.T.; Dong H.; Zavalij P.Y.; Whittingham M.S. Synthesis of Vanadium Oxide Nanofibers and Tubes Using Polylactide Fibers as Template. *Mater. Res. Bull.* **2005**, *40*, 383-393.

(16) Chirayil T.; Zavalij P.Y.; Whittingham M.S. Hydrothermal Synthesis of Vanadium Oxides. *Chem. Mater.* **1998**, *10*, 2629-2640.

(17) Livage J. Hydrothermal Synthesis of Nanostructured Vanadium Oxides. *Materials* **2010**, *3*, 4175-4195.

(18) Chan C. K.; Peng H.; Liu G.; Mcilwrath K.; Zhang X. F.; Huggins R. A.; Cui Y. High-performance Lithium Battery Anodes Using Silicon Nanowires. *Nat. Nanotechnol.* **2008**, *3*, 31-35.

(19) Liu J.; Xia H.; Xue D. F.; Lu L. Double-Shelled Nanocapsules of V_2O_5-Based Composites as High-Performance Anode and Cathode Materials for Li Ion Batteries. *J. Am. Chem. Soc.* **2009**, *131*, 12086-12087.

(20) Mai L. Q.; Xu L.; Han C. H.; Xu X.; Luo L. Z.; Zhao S. Y.; Zhao Y. L. Electrospun Ultralong Hierarchical Vanadium Oxide Nanowires with High Performance for Lithium Ion Batteries. *Nano Lett.* **2010**, *10*, 4750-4755.

(21) S. K. Gao, Z. J. Chen, M. D. Wei, K. M. Wei and H. S. Zhou. Single crystal nanobelts of $V_3O_7 \cdot H_2O$: A Lithium Intercalation Host with a Large Capacity. *Electrochim. Acta* **2009**, *54*, 1115-1118.

(22) Prado-Gonjal J.; Molero-Sánchez B.; Ávila-Brande D.; Morán E.; Pérez-Flores J. C.; Kuhn A.; García-Alvarado F. The Intercalation Chemistry of $H_2V_3O_8$ Nanobelts Synthesised by a Green, Fast and Cost-effective Procedure. *J. Power Sources* **2013**, *232*, 173-180.

(23) Sarkar S.; Bhowmik A.; Pan J.; Bharadwaj M. D.; Mitra S. Preparation, Structure Study and Electrochemistry of Layered $H_2V_3O_8$ Materials: High capacity Lithium-ion Battery Cathode. *J. Power Sources* **2016**, *329*, 179-189.

(24) Wang D.; Wei Q.; Sheng J.; Hu P.; Yan M.; Sun R.; Xu X.; An Q.; Mai L. Flexible Additive Free $H_2V_3O_8$ Nanowire Membrane as Cathode for Sodium Ion Batteries. *Phys. Chem. Chem. Phys.* **2016**, *18*, 12074-12079.

(25) Rastgoo-Deylami M.; Heo J. W.; Hong S.-T. High Potassium Storage Capability of $H_2V_3O_8$ in a Non-Aqueous Electrolyte. *ChemistrySelect* **2019**, *4*, 11711- 11717.

(26) Rastgoo-Deylami M.; Chae M. S.; Hong, S.-T. $H_2V_3O_8$ as a High Energy Cathode Material for Nonaqueous Magnesium-Ion Batteries. *Chem. Mater.* **2018**, *30*, 7464-7472.

(27) Tang H.; Xu N.; Pei C.; Xiong F.; Tan S.; Luo W.; An Q.; Mai L. $H_2V_3O_8$ Nanowires as High-capacity Cathode Materials for Magnesium-based Battery. *ACS Appl. Mater. Interfaces* **2017**, *9*, 28667-28673.

(28) Pang Q.; Sun C.; Yu Y.; Zhao K.; Zhang Z.; Voyles P. M.; Chen G.; Wie Y.; Wang X. $H_2V_3O_8$ Nanowire/Graphene Electrodes for Aqueous Rechargeable Zinc Ion Batteries with High Rate Capability and Large Capacity. *Adv. Energy Mater.* **2018**, *8*, 1800144.

(29) Zhu K.; Yan X.; Zhang Y.; Wang Y.; Su A.; Bie X.; Zhang D.; Du F.; Wang C.; Chen G.; Wie Y. Synthesis of $H_2V_3O_8$/Reduced Graphene Oxide Composite as a Promising Cathode Material for Lithium-Ion Batteries. *ChemPlusChem* **2014**, *79,* 447-453.

(30) Zhang C.; Song H.; Zhang C.; Liu C.; Liu Y.; Cao G. Interface Reduction Synthesis of $H_2V_3O_8$ Nanobelts–Graphene for High-Rate Li-Ion Batteries. *J. Phys. Chem. C* **2015**, *119*, 11391-11399.

(31) Liua Z.; Xu R.; Weia W.; Jing P.; Li X.; Zhu Q.; Sun H.; Dong Y.; Zakharova G. S. Flexible $H_2V_3O_8$ Nanobelts/Reduced Graphene Oxide Electrodes with High Mass Loading for Lithium Ion Batteries. *Solid State Ionics* **2019**, *329*, 74-81.

(32) Simões M.; Mettan Y.; Pokrant S.; Weidenkaff A. Surface-Modified Lithiated $H_2V_3O_8$: A Stable High Energy Density Cathode Material for Lithium-Ion Batteries with $LiPF_6$ Electrolytes. *J. Phys. Chem. C* **2014**, *118*, 14169-14176.

(33) Söllinger D.; Karl M.; Redhammer G. J.; Schoiber J.; Werner V.; Zickler G. A.; Pokrant S. Modified $H_2V_3O_8$ to Enhance the Electrochemical Performance for Li-ion Insertion: The Influence of Prelithiation and Mo-Substitution. *ChemSusChem* **2021**, *14*, 1112-1121.

(34) Söllinger D.; Berger T.; Redhammer G. J.; Schoiber J.; Pokrant S. Chemical Preintercalation of $H_2V_3O_8$-rGO Composites for Improved Na- and Li-ion Battery Cathodes. ChemElectroChem **2021**, *22,* 4223-4232.

(35) Theobald F. ; Cabala R. Hydrate $V_3O_7 \cdot H_2O$. *Comptes Rendus Hebdomadaires Des Seances De L'Academie Des Sciences Serie C* **1970**, *270*, 2138.

(36) Oka Y.; Yao T.; Yamamoto N. Structure Determination of $H_2V_3O_8$ by Powder X-ray Diffraction. *J. Solid State Chem.* **1990**, *89*, 372-377.

(37) Mettan Y.; Caputo R.; Chatterji T. A Theoretical and Experimental Study of the Crystal Structure of $H_2V_3O_8$. *RSC Adv.* **2015**, *5*, 106543-106550.

(38) Tsang C.; Manthiram A. Synthesis of Nanocrystalline VO_2 and Its Electrochemical Behavior in Lithium Batteries. *J. Electrochem. Soc.* **1997**, *144*, 520-524.

(39) Wu Y.; Xu X.; Zhu C.; Liu P.; Yang S.; Xin H. L.; Cai R.; Yao L.; Nie M.; Lei S.; Gao P.; Sun L.; Mai L.; Xu F. In Situ Visualization of Structural Evolution and Fissure Breathing in (De)lithiated $H_2V_3O_8$ Nanorods. *ACS Energy Lett.* **2019**, *4*, 2081-2090.

(40) Hoelzel M.; Senyshyn A.; Juenke N.; Boysen H.; Schmahl W.; Fuess H. High-resolution Neutron Powder Diffractometer SPODI at Research Reactor FRM II. *Nucl. Instr. A* **2012**, *667*, 32-37.

(41) Rodriguez-Carvajal J. Recent Advances in Magnetic Structure Determination by Neutron Powder Diffraction. *Physica B: Condensed Matter* **1993**, *192*, 55-69.

(42) Sears V. F. Neutron Scattering Lengths and Cross Sections. *Neutron News* **1992**, *3*, 26-37.

(43) Momma K.; Izumi F. VESTA 3 for Three-dimensional Visualization of Crystal, Volumetric and Morphology Data. *J. Appl. Crystallogr.* **2011**, *44*, 1272-1276.

(44) Clark S. J.; Segall M. D.; Pickard C. J.; Hasnip P. J.; Probert M. J.; Refson K.; Payne M. C. First Principles Methods Using CASTEP. Z. Kristallogr. **2005**, *220*, 567-570.

(45) Pickard C. J.; Mauri F. All-electron Magnetic Response with Pseudopotentials: NMR Chemical Shifts. *Phys. Rev. B* **2001**, *63*, 245101.

(46) Perdew J. P.; Burke K.; Ernzerhof M. Generalized Gradient Approximation Made Simple. *Phys. Rev. Lett.* **1996**, *77*, 3865-3868.

(47) Yates J. R.; Pickard C. J.; Mauri F. Calculation of NMR Chemical Shifts for Extended Systems Using Ultrasoft Pseudopotentials. *Phys. Rev. B* **2007**, *76*, 024401.

(48) Massiot D., Fayon F., Capron M.; King I.; Le Calvé S.; Alonso B.; Durand J.-O.; Bujoli B.; Gan Z.; Hoatson G.. Modelling One-and Two-dimensional Solid-State NMR Spectra. *Magn. Reson. Chem.* **2002**, *40*, 70-76.

(49) Hellmann I.; Zakharova G.S.; Volkov V.L.; Täschner C.; Leonhardt A.; Büchner B.; Klingeler R. Static Susceptibility and Heat Capacity Studies on $V_3O_7 \cdot H_2O$ Nanobelts. *J. Magn. Magn. Mater.* **2010**, *322*, 878-881.

(50) Pérez-Flores J. C.; García-Alvarado F.; Hoelzel M.; Sobrados I.; Sanz J.; Kuhn A. Insight into the Channel Ion Distribution and Influence on the Lithium Insertion Properties of Hexatitanates $A_2Ti_6O_{13}$ (A = Na, Li, H) as Candidates for Anode Materials in Lithium-ion Batteries. *Dalton Trans.* **2012**, *41*, 14633-14642.

(51) Gornostansky S. D.; Stager C. V. Nuclear Magnetic Resonance Study of V_2O_5. *J. Chem. Phys.* **1967**, *46*, 4959-4962.

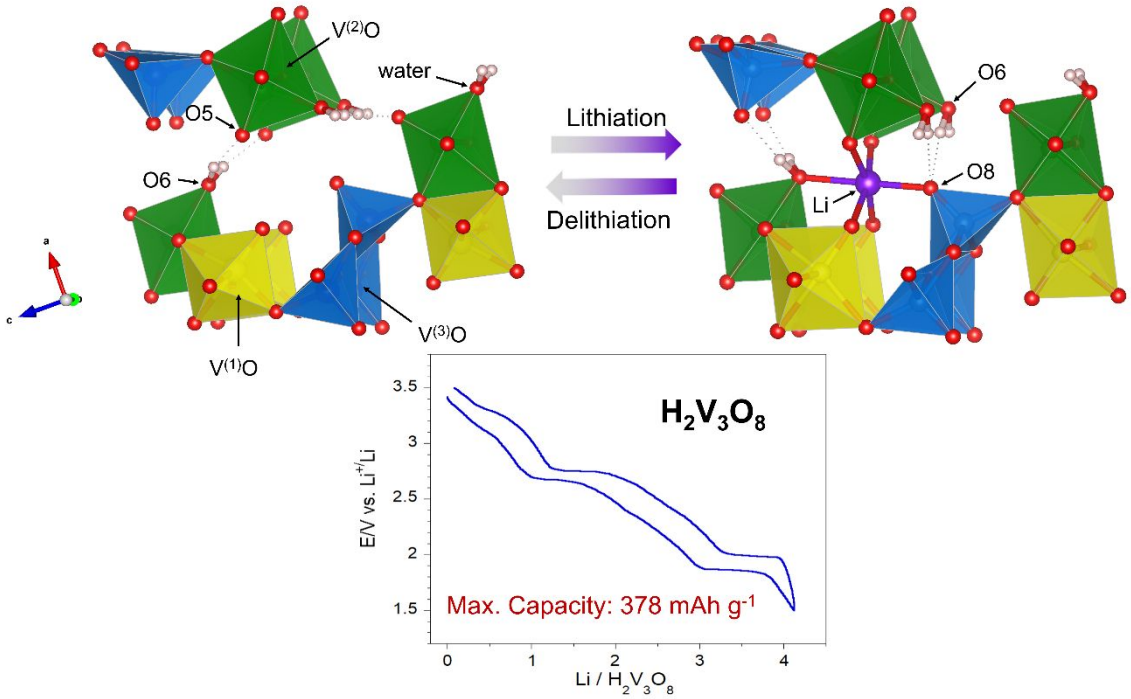
V(2)O
water
O5
O6
V(1)O
V(3)O
Lithiation
Delithiation
O6
O8
Li
a
c
b

H2V3O8
E/V vs. Li+/Li
Max. Capacity: 378 mAh g-1
Li / H2V3O8
3.5
3
2.5
2
1.5
0
1
2
3
4

TOC Graphic

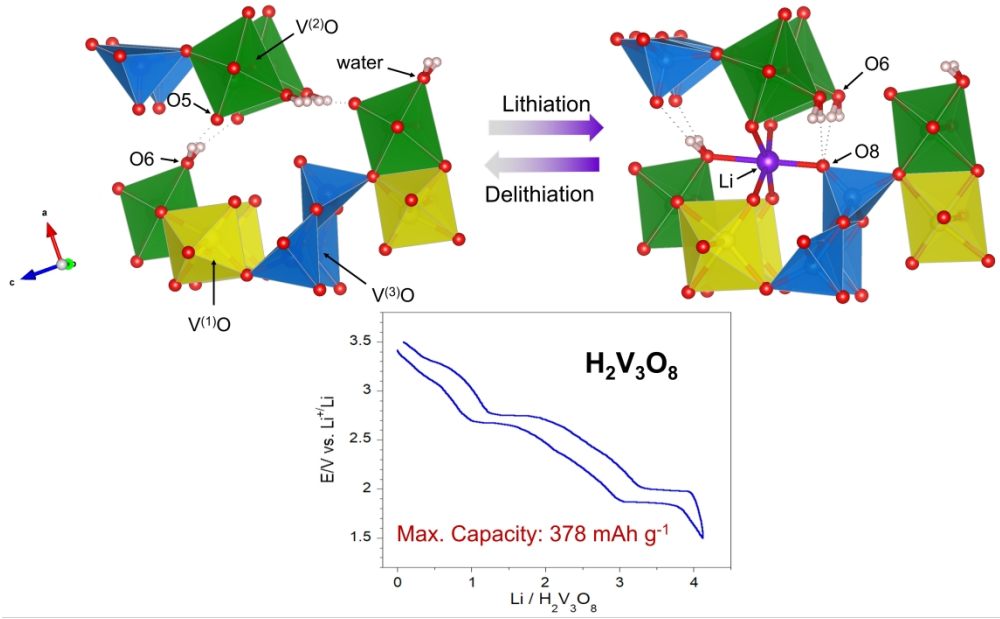

445x277mm (300 x 300 DPI)